

Online Tracking of Varying Inertia using a SDFT Approach

Vanbecelaere Foeke, Derammelaere Stijn, Nevaranta Niko, De Viaene Jasper,
Verbelen Florian, Stockman Kurt, Monte Michael

This is a Post-print version of a publication
published by Elsevier
in Mechatronics

DOI: 10.1016/j.mechatronics.2020.102361

Copyright of the original publication: © Elsevier 2020

Please cite the publication as follows:

Vanbecelaere, F., Derammelaere, S., Nevaranta, N., De Viaene, J., Verbelen, F., Stockman, K., Monte, M. (2020). Online Tracking of Varying Inertia using a SDFT Approach. Mechatronics, vol. 68. DOI: 10.1016/j.mechatronics.2020.102361

**This is a parallel published version of an original publication.
This version can differ from the original published article.**

Online Tracking of Varying Inertia using a SDFT Approach

Foeke Vanbecelaere^{a,d}, Stijn Derammelaere^{a,b,d}, Niko Nevaranta^c, Jasper De Viaene^{a,d}, Florian Verbelen^{a,d}, Kurt Stockman^{a,d}, Michael Monte^{a,d}

^a*Department of Electrical Energy, Metals, Mechanical Constructions and Systems, Ghent University Campus Kortrijk, 8500 Kortrijk, Belgium*

^b*Department of Electromechanics, Op3Mech, University of Antwerp, Groenenborgerlaan 171, 2020 Antwerp, Belgium*

^c*Department of Electrical Engineering, Lappeenranta-Lahti University of Technology, 53850 Lappeenranta, Finland*

^d*Member of EEDT partner of Flanders Make*

Abstract

The mechanical dynamics of modern machines very often depend on the angular position of the driven axis. To obtain optimal control, such applications typically require an advanced control structure such as an adaptive controller. Moreover, the variation in the dynamics like changing inertia, load torque, and viscous friction limits the performance and reduces the energy efficiency. Energy savings can be obtained by using so-called trajectory optimization techniques combined with feedforward control. However, both optimization and adaptive control require the knowledge of the position dependency of the mechanical parameters. In the case of reciprocating mechanisms, for instance, this position dependency is significant. Consequently, the mechanical parameters change rapidly at high operating speed of the machine. This paper thus contributes towards fast and accurate estimation of rapidly varying mechanical parameters. A sliding discrete Fourier transform (SDFT) approach is proposed to track the inertia variation of a reciprocating mechanism online. The feasibility is verified with experiments on an industrial pick and place unit. Both the results on the real machine and its CAD equivalent, modelled in a multibody dynamics software package, are considered. In addition, the developed inertia tracking algorithm is proven to be implementable in standard commercial drive components.

Keywords: Online parameter estimation, inertia variation, sliding discrete Fourier transform (SDFT), motion control, co-simulation

1. Introduction

In modern machines, the mechanical structure driven by an electrical machine has a large influence on the optimal trajectory, control and dimensioning of the electrical actuator. The mechanical parameters of the structure very often depend on the angular position of the driven axis. Reciprocating mechanisms are widely used for machines performing repetitive tasks because they have the advantage that a desired complex movement of the follower linkage is achieved by a simple rotational movement of the driven axis. However, an inherent property is that the reduced load parameters such as the inertia and static torque depend on the position of that driven axis [1]. To avoid oversizing, sub-optimal control and unnecessary energy consumption it is essential to know these variable parameters. Identifying the inertia, among other parameters like load torque and friction is crucial for selection and dimensioning of the motor [2], optimization of the trajectory setpoint [3, 4] and the implementation of adaptive control [5] and feedforward control [6].

In literature, a wide range of parameter and system identification techniques are found. The approach is either based on time- or frequency-domain observations and the identification is either performed online or offline.

The most common offline method is the frequency response identification with a PRBS-signal as additional torque. This is proven to be a successful technique for linear systems [7] and even for non-linear systems in [8]. The known drawback is that the system must remain unchanged during the rather long identification experiment, which means that these methods are only valid for time-invariant systems. The offline frequency methods are thus best suited

for commissioning [9] of slowly varying systems where the parameters change due to wear for example.

Common approaches among the offline time-domain methods are heuristic algorithms. In [10] for example, a particle-swarm algorithm is used for self-commissioning of a non-linear system with backlash. The disadvantage of heuristic algorithms is the extensive tuning and long convergence time. Furthermore, accurate estimates of inertia and friction are achieved with the steady-state response method in [11], which can be considered as a multi-step time-domain procedure. Yet this method, too, is only useful for systems with nearly constant load parameters.

Online approaches are thus required for time-variant systems and are typically performed using a recursive algorithm because of computational efficiency. The most common time-domain approach is the recursive least squares (RLS) algorithm. Accurate results with RLS are achieved in [12] for the estimation of the coefficients of a high-order pulse-transfer function and in [13] for the estimation of frequency responses. In both examples the system parameters are constant and the convergence is rather slow. Faster convergence is obtained in [14] for the estimation of the time-varying coefficients of a second order pulse-transfer function. However, initial guesses of the coefficients with an accuracy of $\approx 80\%$ must be available and the estimated coefficients are not converted into mechanical parameters. This limitation of RLS is also clarified in [15] where the mechanical parameters of a two-mass system are estimated. The RLS is designed for estimation of the coefficients of a pulse-transfer function based on time samples of the input and output signal. How to solve the relations between these coefficients and the mechanical parameters is a complex and time-consuming task, especially for high-order systems.

Kalman filters, known for their excellent noise cancellation, can also be used for online estimation in the time-domain. The performance is proven in [16] where step changes in the load torque of a theoretical two-mass system are

accurately estimated in noisy conditions. Also a high variation of inertia is tracked, but less precise. Next in [17] the parameters of a slider-crank mechanism are estimated online. The cyclic variation of the load torque is tracked accurately at high speed, but again the inertia variation tracking is less precise. Important to note is that in both examples the tuning of the estimation settings is extensive. An initial guess of the parameters is required and the process and measurement noise statistics must be known in advance. Less extensive tuning is obtained in [18] and [19] where the Kalman filter is redesigned to act as a Fourier Transform for online estimation of a frequency response. Yet again, the approach is only accurate for slowly time-varying systems because of the rather long identification time.

Despite the efforts of the mentioned time-domain approaches for online parameter estimation, a trade-off between convergence time and accuracy is inevitable and extensive tuning is necessary. In order to estimate rapidly changing system behaviour, a computationally efficient identification technique without convergence and with noise cancellation is needed. The sliding discrete Fourier transform (SDFT) satisfies that requirement. This technique updates the phase and gain of the system at predefined frequencies at every new time sample [20, 21, 22] without convergence. By analysing the system response at frequencies much lower than high-frequency noise signals, the noise is inherently cancelled. In recent work, this frequency-domain approach has proven to be applicable for online estimation. A few examples are online load angle estimation for stepping motor applications in [23] and online transfer function estimation of a mechanical system with varying dynamics in [24]. Moreover, the computational efficiency is proven in [25] where the estimation algorithm is implemented on a real-time platform.

Motivated by the advantages, this paper proposes the SDFT for tracking of the inherently varying inertia of a reciprocating mechanism. An industrial pick and place unit, shown in figure 1, is used as a proof of concept. The performance and applicability is first tested on a CAD equivalent of the machine

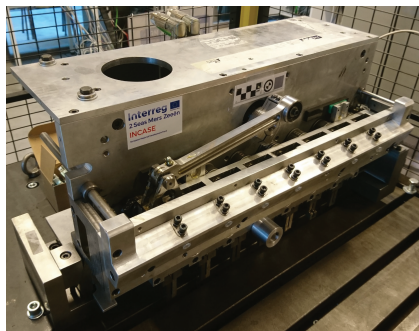


Figure 1: An industrial pick and place unit, existing of a reciprocating mechanism

with a coupled simulation (co-simulation) approach. In a co-simulation, the control algorithm is implemented in e.g. Matlab/Simulink, and the mechanical structure is modelled in CAD software. By implementation of the estimation algorithm in a commercial hardware component, the feasibility is also tested on the real machine. Both the results from the real machine and its CAD equivalent are compared with the inertia calculated from a theoretical model of the machine. This calculation is a complex and time-consuming task and only serves to have a valid reference inertia profile.

The paper is structured as follows. Section 2 shows the theoretical derivation for the reference inertia profile. In section 3, the pick and place unit is simplified to a two-mass system in order to clarify the impact of the varying inertia on the system dynamics. Section 4 explains the principle of the SDFT algorithm and how the algorithm is used to estimate the inertia. In section 5, the estimation is done with co-simulations and the tuning for proper performance is discussed. Finally, validation by measurements are presented in section 6.

2. Theoretical model

A simplified scheme of the machine is shown in figure 2. In the figure, the different joints (A, B, C, D, E, F and G) and linkages are depicted. The mechanism is driven at joint A, resulting in motion of the rotor position θ_1 . The mass and inertia of each individual linkage is constant, but the reduced moment

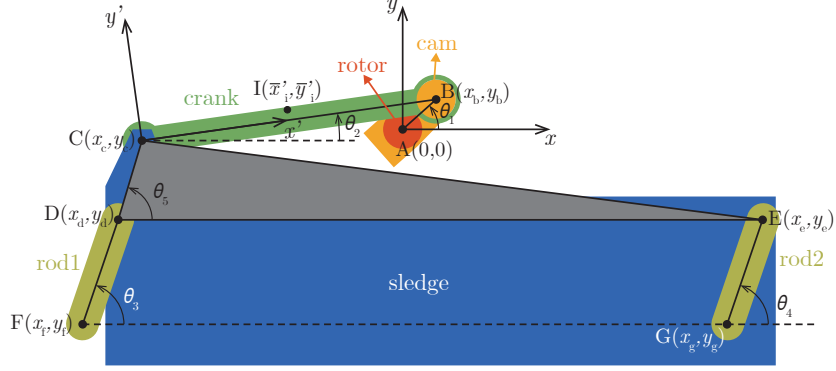


Figure 2: Simplified scheme of the pick and place unit, with its joints and linkages

of inertia at the driven axis varies in function of this position. To determine the reduced load inertia $J_1(\theta_1)$, the kinetic energy of the mechanism is considered. The total kinetic energy E_{tot} resulting from the rotational motion at joint A is written as:

$$E_{\text{tot}} = \frac{1}{2} J_1(\theta_1) \dot{\theta}_1^2 \quad (1)$$

By rewriting (1), it is clear that the inertia $J_1(\theta_1)$ is determined by dividing the kinetic energy E_{tot} by the angular velocity $\dot{\theta}_1$ of the driven axis:

$$J_1(\theta_1) = \frac{2E_{\text{tot}}}{\dot{\theta}_1^2} \quad (2)$$

The total kinetic energy E_{tot} equals the sum of the kinetic energy of each linkage:

$$E_{\text{tot}} = E_{\text{cam}} + E_{\text{crank}} + E_{\text{sledge}} + E_{\text{rod1}} + E_{\text{rod2}} \quad (3)$$

Rod1 rotates around the fixed joint F with angular velocity $\dot{\theta}_3$, rod2 rotates around the fixed joint G with angular velocity $\dot{\theta}_4$ and the cam rotates around the fixed joint A with angular velocity $\dot{\theta}_1$.

$$E_{\text{rod1}} = \frac{1}{2} J_{\text{rod1}} (\dot{\theta}_3)^2 \quad E_{\text{rod2}} = \frac{1}{2} J_{\text{rod2}} (\dot{\theta}_4)^2 \quad E_{\text{cam}} = \frac{1}{2} J_{\text{cam}} (\dot{\theta}_1)^2 \quad (4)$$

The sledge performs a translational motion at joint C.

$$E_{\text{sledge}} = \frac{1}{2} m_{\text{sledge}} (\dot{x}_c^2 + \dot{y}_c^2) \quad (5)$$

The crank rotates around joint C with angular velocity $\dot{\theta}_2$, while joint C translates in the x -direction with velocity \dot{x}_c and in the y -direction with velocity \dot{y}_c . With the motion of the crank considered according to its local $x'y'$ -frame (as depicted in figure 2), the kinetic energy is determined [26]:

$$E_{\text{crank}} = \frac{1}{2}m_{\text{crank}}(\dot{x}_c^2 + \dot{y}_c^2) - m_{\text{crank}}\dot{x}_c'\dot{\theta}_2\bar{y}_1' + m_{\text{crank}}\dot{y}_c'\dot{\theta}_2\bar{x}_1' + \frac{1}{2}J_{\text{crank}}(\dot{\theta}_2)^2 \quad (6)$$

In (6), \bar{x}_1' and \bar{y}_1' are the coordinates of the centre of mass I according to the $x'y'$ -frame. \dot{x}_c' and \dot{y}_c' are the components of the velocity of joint C with respect to the same $x'y'$ -frame. As shown in figure 2, the local $x'y'$ -frame is rotated with an angle θ_2 according to the global xy -frame. After transforming to the global frame, the kinetic energy of crank C is found:

$$E_{\text{crank}} = \frac{1}{2}m_{\text{crank}}(\dot{x}_C^2 + \dot{y}_C^2) - m_{\text{crank}}(\dot{x}_C\cos(\theta_2) + \dot{y}_C\sin(\theta_2))\dot{\theta}_2\bar{y}_1' + m_{\text{crank}}(-\dot{x}_C\sin(\theta_2) + \dot{y}_C\cos(\theta_2))\dot{\theta}_2\bar{x}_1' + \frac{1}{2}J_{\text{crank}}(\dot{\theta}_2)^2 \quad (7)$$

With kinematic analysis, the position and velocity of all joints are written in function of the position θ_1 and velocity $\dot{\theta}_1$ of the driven joint A . The derivation of the kinematic relations is described in the appendix 8.1.

By substitution of the kinematic relations in (4), (5) and (7), the kinetic energy of each link is obtained in function of the position θ_1 and velocity $\dot{\theta}_1$ of the driven axis. After taking the sum, as shown in (3), dividing it by the angular velocity $\dot{\theta}_1$ and rewriting, the equation for the reduced load inertia $J_l(\theta_1)$ is obtained:

$$\begin{aligned} J_l(\theta_1) = & J_{\text{cam}} + J_{\text{crank}} \left(\frac{|AB|}{|CB|} \right)^2 \left(\frac{\sin(\theta_1 - \theta_3)}{\sin(\theta_2 - \theta_3)} \right)^2 \\ & + (J_{\text{rod1}} + J_{\text{rod2}}) \left(\frac{|AB|}{|FD|} \right)^2 \left(\frac{\sin(\theta_1 - \theta_2)}{\sin(\theta_3 - \theta_2)} \right)^2 \\ & + (m_{\text{crank}} + m_{\text{sledge}})|AB|^2 \left(\left(\frac{\sin(\theta_1 - \theta_3)}{\sin(\theta_2 - \theta_3)} \right)^2 - \frac{\sin(2\theta_1 - \theta_2 - \theta_3)}{\sin(\theta_2 - \theta_3)} \right) \\ & - 2\bar{y}_1'm_{\text{crank}} \frac{|AB|^2}{|CB|} \left(\frac{\sin(\theta_1 - \theta_3)\sin(\theta_2 - \theta_1)}{\sin(\theta_2 - \theta_3)} \right) \\ & + \bar{x}_1'm_{\text{crank}} \frac{|AB|^2}{|CB|} \left(\frac{\sin(\theta_1 - \theta_3)}{\sin^2(\theta_2 - \theta_3)} (\sin(2\theta_2 - \theta_1 - \theta_3) - \sin(\theta_1 - \theta_3)) \right) \end{aligned} \quad (8)$$

For convenience of the kinematic analysis, the rotor position θ_1 is defined according to the global xy -frame with a positive angle in counter clockwise direction. But as depicted in figure 3, this definition does not agree with the machine position θ . The origin of θ is located at an angle δ with a positive angle in clockwise direction. The reduced inertia $J_1(\theta)$ in function of the machine position θ is thus found by substitution of $\theta_1 = \delta - \theta$ in (8). The theoretical reference is plotted in figure 4. The reference is valid because it results from the fundamental laws of energy conservation. Note that the maximum inertia is about 18 times the minimum inertia.

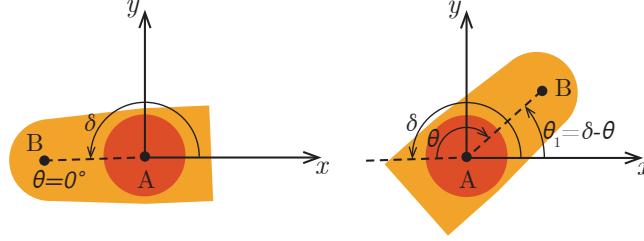


Figure 3: The machine in starting position (left) and in a certain position θ (right)

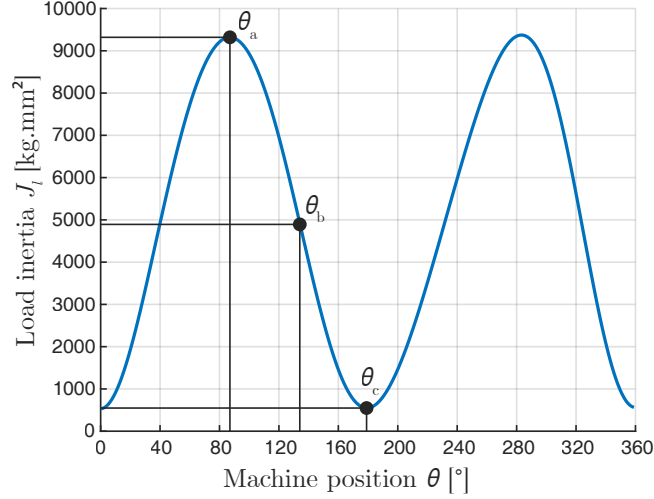


Figure 4: Analytical calculation (8) of the reduced load inertia $J_1(\theta)$

3. Influence of inertia in the frequency domain

3.1. Simplification to a two-mass system

To clarify the influence of the load inertia on the mechanical dynamics, a simplified model of the industrial pick and place unit is defined. With a standard procedure in the drive software, described in the drive manual [27], the gain characteristic of the real machine is identified at the position θ_a of high inertia (see figure 4). The choice of this position is justified later in section 3.2. The measured gain is shown in figure 5. Note that during the measurement the system behaviour is not linear. Although the system parameters are nearly constant because of the constant position setpoint, the velocity goes through zero due to the added frequency-rich torque signal. As a result, static friction is not negligible, leading to a biased frequency response. Despite the non-linear effects, a clear pair of antiresonance and resonance is present. Representing the machine as a two-mass system is thus a logical simplification [28, 29]. In figure 6, a schematic representation of this simplified model is shown. The simplification assumes that the driven rotor represented with the rotor inertia

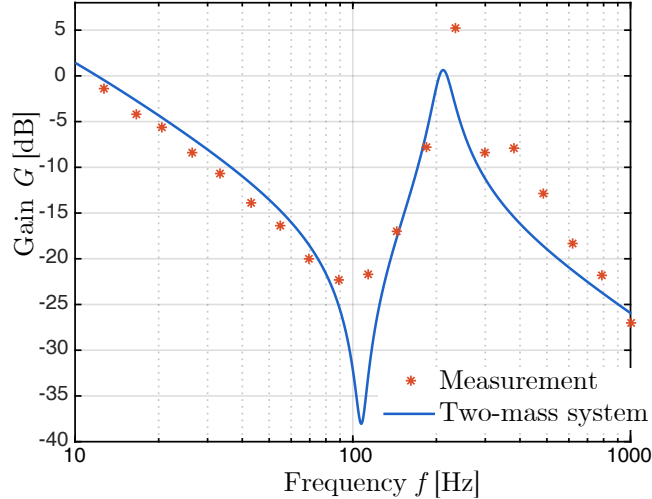


Figure 5: Measured and calculated frequency response of the pick and place unit and the simplified two-mass system

J_r is connected with the load by a spring-damper coupling. The stiffness of the spring is represented with k and b is the damping coefficient of the damper. The load is assumed to be the equivalent of all rigidly connected linkages, except the rotor, and is represented with the load inertia J_l . The rotor and load damping are represented respectively with b_r and b_l .

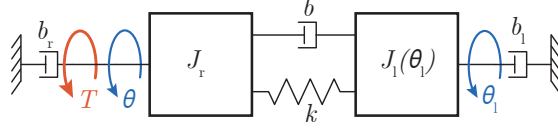


Figure 6: Model of a damped two-mass system

The dynamics are described with the differential equations shown in (9). After Laplace transformation of (9), the transfer function describing the dynamic influence of the torque T on the velocity $\dot{\theta}$, is found in (10).

$$\begin{cases} T - b_r \dot{\theta} - b(\dot{\theta} - \dot{\theta}_l) - k(\theta - \theta_l) = J_r \ddot{\theta} \\ -b_l \dot{\theta}_l + b(\dot{\theta} - \dot{\theta}_l) + k(\theta - \theta_l) = J_l \ddot{\theta}_l \end{cases} \quad (9)$$

$$\frac{\dot{\theta}(s)}{T(s)} = \frac{J_l s^2 + (b + b_l)s + k}{J_r J_l s^3 + ((J_r + J_l)b + J_r b_l + J_l b_r)s^2 + ((J_r + J_l)k + b_r b_l + (b_r + b_l)b)s + (b_r + b_l)k} \quad (10)$$

Realistic values of the mechanical parameters in (10) are listed in Table 1. The value of the rotor inertia J_r is found in the data-sheet of the motor. The value of the load inertia J_l is read from the inertia profile in figure 4 at the position θ_a of high inertia. The other parameters k , b , b_r and b_l are found by fitting the measured gain characteristic with the gain of (10) with a manual trial and error approach. The result is shown in figure 5 with the mechanical parameters listed in Table 1.

Table 1: Mechanical parameters of the simplified two-mass system

J_r	3200 kg·mm ²
k	4221 Nm/rad
b	0.396 Nms/rad
b_r	0.2 Nms/rad
b_l	0.1 Nms/rad

3.2. Frequency regions of interest

The gain characteristics according to (10) for selected values of the load inertia J_l and the constants in Table 1 are plotted in figure 7 in solid lines. The three selected values are the maximum inertia at position θ_a , an average inertia at position θ_b and the minimum inertia at position θ_c . The values are depicted in figure 4 and listed in Table 2.

Table 2: Selected values of the load inertia J_l out of figure 4

	Position θ [°]	Inertia J_l [kg·mm ²]
θ_a	87	9319
θ_b	134	4927
θ_c	179	548

For each inertia value, the gain according to its equivalent pure inertial load is plotted in a dashed line of -20 dB/dec. The transfer function of this rigid undamped system is found by substitution of $\theta = \theta_l$ and $b_r = b_l = 0$ in (9):

$$\frac{\dot{\theta}(s)}{T(s)} = \frac{1}{(J_r + J_l)s} \quad (11)$$

Also in a dashed line, the gain of a pure inertial load existing of only the rotor inertia J_r is plotted. A final characteristic is the static gain $|G(s=0)|$ of (10) in a dotted line.

A first observation is that for each characteristic, a range of frequencies is found where the gain according to the two-mass system (10) equals the gain

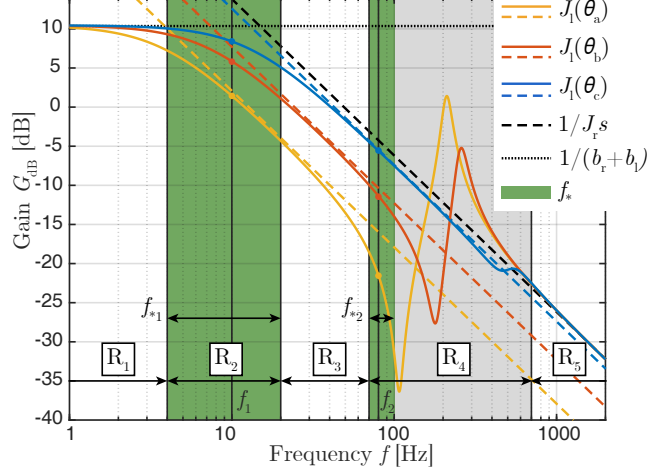


Figure 7: Gain characteristic for the selected values of the load inertia J_l in solid lines and their equivalent pure inertial load in dashed lines. The regions of interest f_* in green are suitable for inertia estimation.

according to its pure inertial load (11). This means that for these frequencies the gain is only influenced by the rotor inertia J_r and load inertia J_l . Unfortunately this region is not the same for all characteristics. At 20 Hz for example, the gain of $J_l(\theta_a)$ equals the slope of -20 dB/dec but not for $J_l(\theta_b)$ and $J_l(\theta_c)$.

By observing the deviation of the slope of -20 dB/dec, the frequency range can be divided in 5 regions. In each region, the gain of the two-mass system is influenced by different mechanical parameters. As summarized in Table 3, R_2 and R_4 are the remaining regions of interest because of the reduced number of describing parameters.

Region R_2 is considered as the first frequency region f_{*1} of interest where the system is described as a damped one-mass system:

$$\frac{\dot{\theta}(s)}{T(s)} = \frac{1}{(J_r + J_l)s + (b_r + b_l)} \quad (12)$$

If the gain is measured inside f_{*1} for varying positions, the load inertia J_l is determined by converting the gain of (12) with a known value of the rotor inertia J_r and the sum of the damping factors b_r and b_l .

The transfer function in region R_4 , is found by substituting $b_r = b_l = 0$ in

Table 3: Observations from the gain characteristics of the two-mass system

	Parameters	Observation
R ₁	b_r, b_l	The gain at θ_c equals the static gain $ G(s=0) $.
R ₂	J_r, J_l, b_r, b_l	At all positions, the slope deviates due to external damping and not due to the spring-damper coupling.
R ₃	J_r, J_l, b_r, b_l, k, b	At θ_c the slope deviates due to external damping and at θ_a the slope deviates due to the spring-damper coupling.
R ₄	J_r, J_l, k, b	At all positions, the slope deviates due to the spring-damper coupling.
R ₅	J_r	At all positions, the gain equals the pure inertial load of the rotor. The spring-damper coupling is not able to respond to the high frequency input torque and the load inertia is not moving.

the transfer function (10) of the two-mass system:

$$\frac{\dot{\theta}(s)}{T(s)} = \frac{J_l s^2 + bs + k}{J_r J_l s^3 + (J_r + J_l)bs^2 + (J_r + J_l)ks} \quad (13)$$

However, the slope of the gain between the antiresonance at position θ_a and the resonance at position θ_c is very different for varying positions. At 200 Hz for example, the slope at position θ_a and θ_b is positive while being negative at position θ_c . By limiting region R₄ until a frequency slightly before the antiresonance at position θ_a , a second region of interest f_{*2} is found. If the gain is measured inside f_{*2} , the load inertia J_l is known by converting the gain of (13) with the rotor inertia J_r , stiffness k and damping b as prior known parameters.

3.3. Conversions from gain to inertia

As concluded previously with figure 7, the varying load inertia J_l can be tracked by measuring the gain at varying positions. After calculation of the

modulus of the transfer function (12), which is valid for frequencies inside the region of interest f_{*1} , the conversion from gain G to load inertia J_l is found:

$$J_l = \frac{1}{\omega} \left(\sqrt{\frac{1}{G^2} - (b_r + b_l)^2} \right) - J_r \quad (14)$$

Note that the frequency f is represented in (14) with $\omega = 2\pi f$ and that in figure 7 the gain G is represented in dB:

$$G_{\text{dB}} = 20 \log(G) \quad (15)$$

For frequencies inside the region of interest f_{*2} , the gain conversion is found in a similar way from the modulus of the transfer function in (13):

$$\begin{aligned} J_l &= \frac{A + \sqrt{B}}{C} \\ A &= (k - b^2)G^2 J_r \omega^3 - (G^2 J_r k^2 + 1)k\omega \\ B &= -G^4 J_r^4 b^2 \omega^8 + 2G^2 J_r^2 b^2 \omega^6 + (G^2 b^2 - 1)b^2 \omega^4 + 2G^2 b^2 k^2 \omega^2 + G^2 k^4 \\ C &= G^2 J_r^2 \omega^5 - (2G^2 J_r k - G^2 b^2 + 1)\omega^3 + G^2 k^2 \omega \end{aligned} \quad (16)$$

4. The SDFT approach

4.1. The SDFT algorithm

As concluded in the previous section 3, the inertia can be tracked for varying positions if the frequency response at one specific frequency is measured. To do so, the SDFT is of interest. This algorithm can determine frequency responses at consecutive time stamps in a computationally efficient manner. Fourier analysis can be used to determine fundamental components of a measured signal. At a discrete time instance k the h^{th} harmonic component $X_h(k)$ based on a period of N samples can be written as:

$$X_h(k) = \sum_{l=0}^{N-1} x(k - (N-1) + l) e^{-j h \frac{2\pi}{N} l} \quad (17)$$

As illustrated in figure 8, one signal period of N samples is needed to calculate the fundamental component. When a new measurement sample is available,

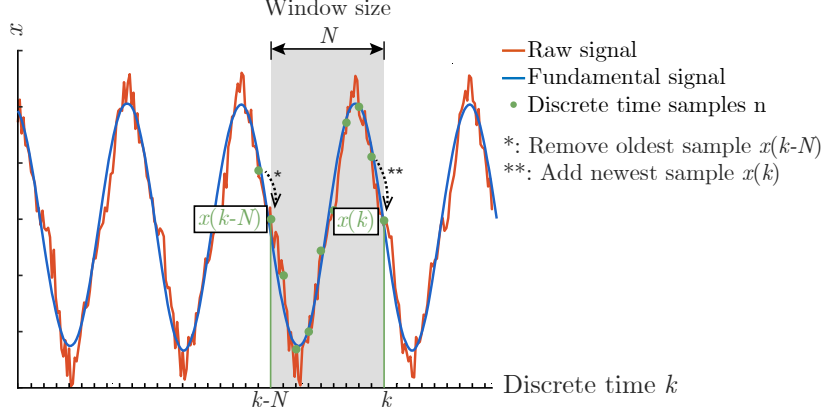


Figure 8: Principle of the DFT applied on a sliding window [21]

(17) could be reconsidered to update the fundamental component. Summing all measurement samples over one signal period according to (17) is time consuming. However, at each new time instance n only the last sample $x(n)$ is added and the oldest sample $x(n - N)$ is removed from the window. This appealing property, which is exploited in [20, 21, 22], is used to implement the frequency response estimation in a computationally efficient manner. The Fourier component $X_h(k)$ at time instance k is written as:

$$X_h(k) = x(k - (N - 1)) + x(k - (N - 1) + 1)) e^{-j\frac{2\pi}{N}} + x(k) e^{-j\frac{2\pi}{N}(N-1)} \quad (18)$$

While the previous component $X_h(k - 1)$ is written as:

$$X_h(k-1) = x(k - N) + x(k - (N - 1)) e^{-j\frac{2\pi}{N}} + x(k - 1) e^{-j\frac{2\pi}{N}(N-1)} \quad (19)$$

After subtraction of (19) from (18):

$$X_h(k) = (X_h(k - 1) - x(k - N)) e^{j\frac{2\pi}{N}} + x(k) e^{j\frac{2\pi}{N}(N-1)} \quad (20)$$

Moreover:

$$e^{j\frac{2\pi}{N}} = e^{-j\frac{2\pi}{N}(N-1)} \quad (21)$$

Finally, (20) is rewritten as:

$$X_h(k) = (X_h(k-1) + x(k) - x(k-N)) e^{j\frac{2\pi}{N}h} \quad (22)$$

For clarification, (22) is represented graphically in figure 9. Note that (22) can be interpreted as the angular shift of the previous Fourier component $X_h(k-1)e^{j2\pi h/N}$ minus the oldest sample $x(k-N)$ plus the most recent sample $x(k)$. This SDFT approach is particularly interesting when only a limited number of Fourier components $X_h(k)$ needs to be known. This is the case here as only one frequency, and therefore one fundamental component is considered.

Figure 9 and (22) illustrate that regardless of the window length N , the

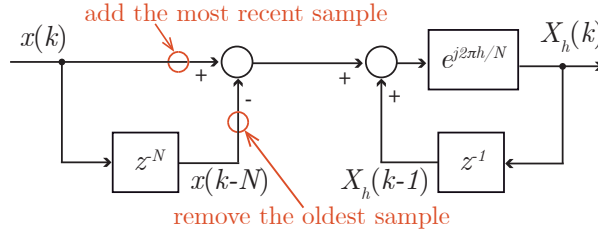


Figure 9: Implementation of the SDFT algorithm [21]

SDFT only needs to determine one real sum, one complex sum and one complex multiplication to compute a successive DFT output. The SDFT is obviously computationally efficient.

4.2. Inertia estimation

Figure 10 shows how the SDFT algorithm and the conversion from gain to inertia are combined to obtain an online inertia estimation. First of all, a controller is designed with the objective that the closed-loop mechatronic system is able to maintain constant speed under varying dynamics. This setpoint of constant speed $\dot{\theta}^*$ is chosen with the intention to track the inertia profile with a constant resolution. Because of the fixed discrete sample time t_s and a constant speed, the resolution $\Delta\theta$ of the position is also fixed. At a certain time t , the

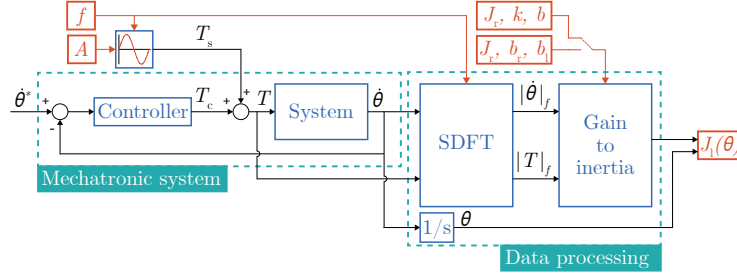


Figure 10: Principle of inertia estimation

resolution $\Delta\theta$ is found as:

$$\Delta\theta(t) = \theta(t) - \theta(t - t_s) \quad (23)$$

Because the approach requires that the gain is tracked at a well-chosen frequency f , both the input signal T and output signal $\dot{\theta}$ must contain a fundamental component at this frequency f . This is achieved by adding an additional sinusoidal torque T_s with a frequency f and amplitude A , resulting in an input torque T that equals $T_c + T_s$. Next, both the input signal T and output signal $\dot{\theta}$ of the system are filtered by the SDFT algorithm, shown in figure 9 to obtain the amplitude at frequency f for both input and output. The gain G is then found as:

$$G = \frac{|\dot{\theta}|_f}{|T|_f} \quad (24)$$

Finally, by converting the measured gain G , the load inertia J_1 is found in function of time. By taking the actual position θ into account, the load inertia J_1 is found in function of the position θ . Depending on the selected frequency f , the conversion is either according to (14) with J_r , b_r and b_1 as prior known mechanical parameters or according to (16) with J_r , k and b as prior known parameters. The inertia is thus calculated at every new time sample without convergence.

Guidelines for tuning of the amplitude A , the speed setpoint $\dot{\theta}^*$, and selecting the frequency f are presented in the next section 5.

5. Co-simulation

5.1. Working principle

During the design phase of a machine, a CAD model is often available. In this paper, Siemens NX is used to model the industrial pick and place unit. Siemens NX, among other CAD packages, delivers the possibility to represent the mechanical system in Matlab/Simulink. This representation is also called a plant. Global simulation of both the controller modelled in Simulink and the mechanical system modelled in Siemens NX, is then possible. This technique of combining two different software packages is called a co-simulation. To clarify the working principle of the proposed estimation method, a model is build in Simulink existing of the algorithm in figure 10. The system is now replaced with the plant of the CAD equivalent of the real machine.

Without the additional sinusoidal torque activated, a standard PI-controller C_{PI} is designed to maintain stable constant speed under varying dynamics:

$$C_{PI} = K_p(1 + K_i \frac{1}{s}) \quad (25)$$

The values $K_p = 1.1$ and $K_i = 50$ are found by obtaining a closed-loop bandwidth 6 times lower than the antiresonance of the open-loop system in figure 5. The step response for $\dot{\theta}^* = 180^\circ/\text{s}$ is shown in figure 11. The

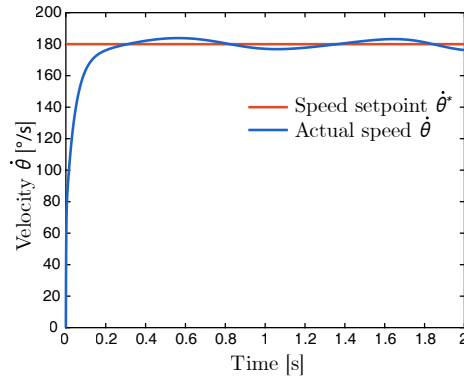


Figure 11: Step response without the added torque signal

fluctuations around the setpoint confirm the desired stable operation of the system under varying dynamics.

To illustrate the influence of the added torque on the input and output signals of the system, a simulation is performed with a sampling time t_s of 0.25 ms, which corresponds to the sampling time of the real-time platform used for controlling the real machine. The other settings are a speed setpoint of $\dot{\theta}^* = 180^\circ/\text{s}$, a frequency $f = 10$ Hz and amplitude $A = 10$ Nm of the sinusoidal torque. The amplitude A is chosen from the static torque that varies between -0,6 and 0,6 Nm due to gravity. In order to have a system response at frequency f due to the load inertia, the amplitude A should be significantly more than the static torque while considering the maximum motor torque T_{\max} of 41.6 Nm.

The input torque is shown in figure 12, the output speed in figure 13 and the position in figure 11. As desired, both the low frequency signal due to the inertia variation and the added frequency signal due to the sinusoidal torque

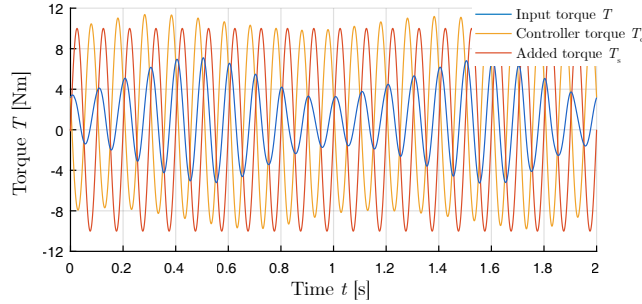


Figure 12: Input torque, which is the sum of the controller torque and the added torque

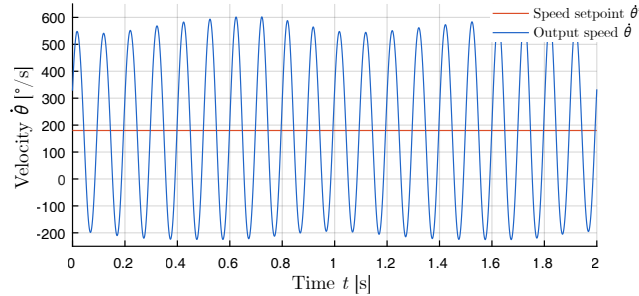


Figure 13: Output speed and the speed setpoint

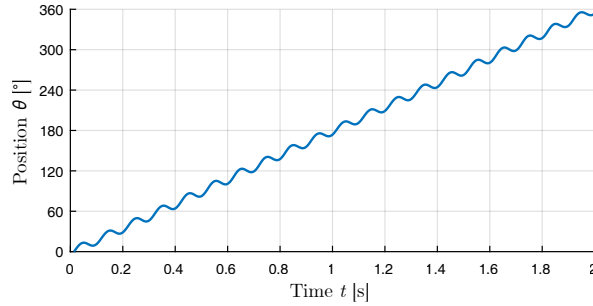


Figure 14: Output position

are clearly present. The fluctuations around the desired speed are larger than the ones in figure 11 due to the added torque. This is also clearly visible in the position of the system. Consequently, the inertia is tracked with a varying resolution $\Delta\theta$ and not with the intention to have a constant resolution. This property is taken into account for further analysis in the next sections where the performance of the SDFT approach is investigated for different values of the speed setpoint $\dot{\theta}^*$ and the excitation frequency f .

5.2. Selection of the additional excitation frequency

Figure 15 shows the results of three simulations with the same speed setpoint of $\dot{\theta}^* = 180^\circ/\text{s}$, the same amplitude $A = 11.86 \text{ Nm}$ and three different frequencies f . The value $A = 11.86 \text{ Nm}$ is chosen to be the same value as used in the measurements section 6. The value $f = 10 \text{ Hz}$ is chosen in the first frequency region of interest f_{*1} , see figure 7, where the gain is converted according to (14). In that case, the prior known parameters are the rotor inertia J_r , the rotor damping b_r and load damping b_l . The next value $f = 80 \text{ Hz}$ is chosen in the second frequency region of interest f_{*2} where the gain is converted according to (16). The prior known parameters in that region are the rotor inertia J_r , the flexibility k and damping b of the coupling. For the next value of $f = 160 \text{ Hz}$ the same conversion (16) is needed.

The results show that only in the case of $f = 80 \text{ Hz}$, a clear correspondence between the estimated inertia and the theoretical reference obtained with (8) is

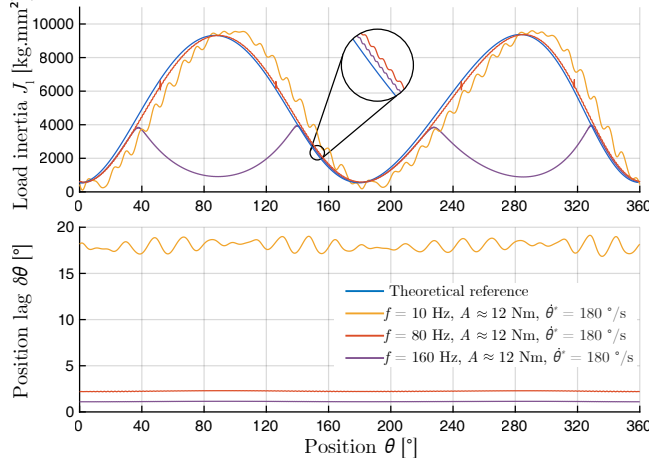


Figure 15: Influence of the frequency f on the inertia estimation

found. The result obtained with $f = 10$ Hz shows that the shape of the profile is correct, despite a clear tracking error and fluctuations.

In the case of $f = 160$ Hz the load inertia is only accurately tracked at positions of low inertia. This confirms that although the same prior known parameters as in $f = 80$ Hz are needed for the conversion (16), the frequency must be chosen inside region f_{*2} . Figure 7 shows that the antiresonance at different positions shifts to the left if the inertia increases. If the frequency is chosen above the antiresonance frequency at high inertia, the gain is not situated before the antiresonance for all positions and thus not correctly converted.

Together with the close-up view in figure 15, it is also clear that the lower the frequency f , the higher the tracking error. This is explained by considering the lagging behaviour of the SDFT algorithm [20]. As described in [23] and illustrated in figure 8 it takes one full SDFT window, existing of N samples, to obtain a completely updated SDFT result and thus an inertia value after conversion. In this case the time window δt is equal to the period of the additional torque T_s :

$$\delta t = \frac{1}{f} = N t_s \quad (26)$$

In figure 16 a close-up view of the output position in figure 14 is shown. At time

t_k , the full window from t_{k-N} until t_k is needed to obtain a result. Since the inertia is estimated in function of the position, this time window $\delta t = t_k - t_{k-N}$ is transformed to a position window $\delta\theta$:

$$\delta\theta = \theta(t_k) - \theta(t_{k-N}) \quad (27)$$

This position window is also called a position lag because it is a result of the lagging behaviour of the SDFT. Due to the obvious oscillations of the position, the position lag $\delta\theta$ is variable.

The first consequence is that the estimated inertia profile lags according to the position lag $\delta\theta$. This is clearly visible in figure 15 in the case of $f = 10$ Hz. The higher the frequency f , the lower the time window δt , the higher the position lag $\delta\theta$. This lagging error is a known error because the position is measured and therefore compensation is possible.

The second consequence of the position lag is clarified with the help of the theoretical inertia profile in figure 17. During a certain position lag $\delta\theta$, the load inertia J_l is variable. This means that for every window of the SDFT, an averaged inertia \hat{J}_l is estimated which is not the correct value. The higher the lag $\delta\theta$, the larger this averaging error. This consequence is represented with oscillations in the inertia profile, which is clearly visible at $f = 10$ Hz in figure 15. Because the load inertia is to be estimated, this error is unknown and cannot

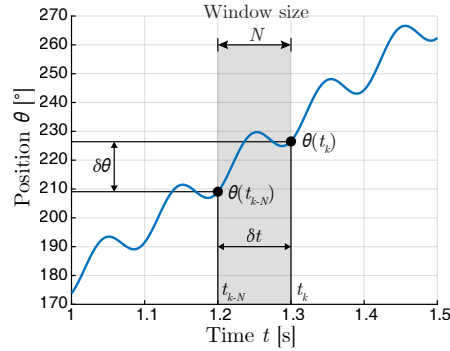


Figure 16: Transformation from time window to position window

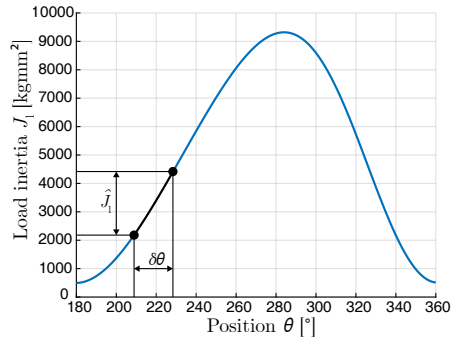


Figure 17: Averaged inertia due to the position lag

be compensated.

Due to the uncorrectable averaging error it can be concluded that choosing the frequency in the lower region f_{*1} is not of interest for fast and accurate estimation of the rapidly changing inertia. By choosing the frequency f higher in region f_{*2} , the time window of the SDFT is smaller leading to more accurate results.

A final important condition for the selection of the frequency f relates to the fact that the SDFT-algorithm is a discrete algorithm with a sample time t_s . Therefore, the number of samples N of the SDFT-window must be an integer value and more than 20 for accurate reproduction of the sine wave at frequency f :

$$N = \frac{1}{ft_s} \geq 20 \quad (28)$$

5.3. Influence of the speed setpoint

Continuing with an additional frequency f of 80 Hz, the influence of the speed setpoint $\dot{\theta}^*$ is investigated. Figure 18 shows the results of two simulations with the same amplitude $A = 11.86$ Nm and two different values of the speed setpoint $\dot{\theta}^*$.

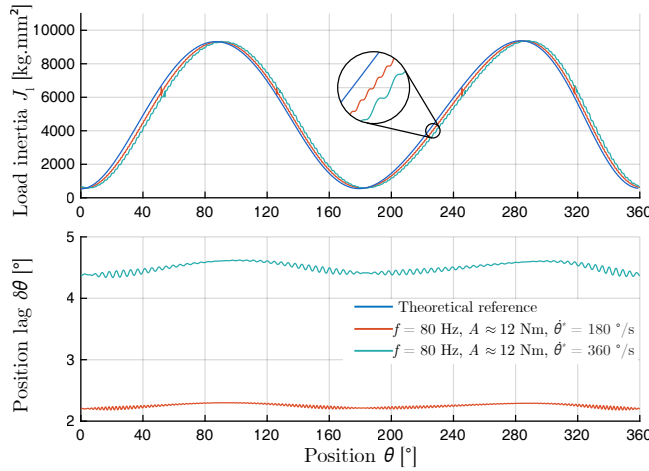


Figure 18: Influence of the speed setpoint $\dot{\theta}^*$ on the inertia estimation

Again, the lagging behaviour is clear. The higher the speed setpoint, the higher the position lag and thus the higher the tracking error. This conclusion is explained by looking at the average slope in figure 16. The figure shows the average slope for a speed setpoint of $180^\circ/\text{s}$. If this setpoint is doubled, the slope and consequently the position lag $\delta\theta$ is also doubled for the same time window δt .

The achievable accuracy of the estimated inertia profile hence depends on the operating speed of the machine. The higher the speed, the less accurate the result and vice versa. Figure 18 however shows that a full inertia profile with a maximum value of 18 times the minimum value is accurately estimated within 1 s. This validates that the proposed SDFT method contributes towards fast and accurate estimation of rapidly varying mechanical parameters.

5.4. Sensitivity of the prior known mechanical parameters

A drawback is that the proposed SDFT method requires that three mechanical parameters are known in advance. An exact value of the rotor inertia J_r is easily found in a data-sheet of the motor. But finding exact values for the flexibility k and damping b of the spring-damper coupling might be a difficult task in practice. As mentioned in section 3.1 an option is to find k and b by fitting a measured gain characteristic to the transfer function of a damped two-mass system. Because the measurement inherently contains non-linearities, the manual fitting procedure leads to an uncertain guess. This uncertainty of both k and b is taken into account by presenting the sensitivity analysis in figure 19. In the analysis, the roughly found values of k and b are considered to be the exact values of the system model.

In the figure, the reference inertia profile is plotted together with an estimated profile with exact values of k and b and settings $f = 80 \text{ Hz}$, $\dot{\theta}^* = 360^\circ/\text{s}$ and $A = 11.86 \text{ Nm}$. In the upper plot, the sensitivity related to k is observed by including estimations with the exact value of b and adjusted values of $k \pm 5\%$ and $k \pm 10\%$. In the lower plot, the sensitivity related to b is observed by including estimations with the exact value of k and adjusted

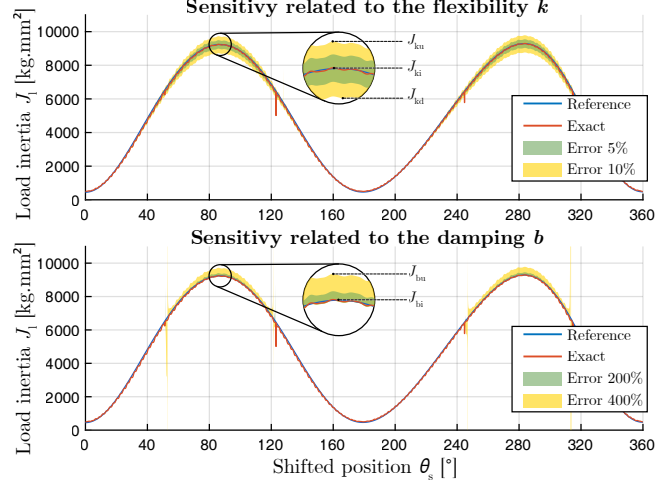


Figure 19: Sensitivity related to uncertain values of the flexibility k and damping b .

values of $b \pm 200\%$ and $b \pm 400\%$ with a lower boundary of $b = 0$. Obviously, negative values of the damping b do not exist in practice.

For convenience, the estimated profiles J_l are corrected with the position lag $\delta\theta$ and are thus shifted:

$$J_l(\theta_s) = J_l(\theta - \delta\theta) \quad (29)$$

The figure shows that at positions of low inertia a wrong guess of k and b does not result in a wrong estimation of the load inertia. The reason for that is clarified with the observations from the gain characteristic in figure 7 in section 3.2. Rough guesses of k and b only affect the estimation at high inertia.

A next conclusion is that the flexibility k is the most sensitive parameter. While an error of $k \pm 10\%$ results in an inaccuracy of $(J_{ku} - J_{kd})/J_{ki} \approx 11\%$, it takes an error of $b + 400\%$ to have an inaccuracy of only $(J_{bu} - J_{bi})/J_{bi} \approx 5\%$.

6. Measurements

To enable online tracking of the varying inertia of the real machine, the Simulink code used for co-simulation in figure 10 is implemented in the real-time hardware target. The implementation is carried out with the PLC

Beckhoff/TwinCAT environment. The system in figure 10 is now replaced with the equivalent input and output signals of the PLC in torque mode. As mentioned, the fixed sample time t_s of the real-time platform is 0.25 ms.

The measurement settings are based on the investigated tuning rules with the co-simulation approach and are listed in Table 4. In the TwinCAT environment,

Table 4: Measurement settings

	A [Nm]	f [Hz]	$\dot{\theta}^*$ [°/s]
1	11.86	80	180
2	11.86	80	360
3	11.86	160	180

the amplitude is specified as a percentage of the maximum motor torque. For all measurements this value is set to 28.5%, resulting in an amplitude A of 11.86 Nm. For illustration, a badly chosen frequency $f = 160$ Hz is included.

For the measurement with index 1, the input and output signals are shown in figures 20, 21 and 22. Figure 20 shows the torque T_m and figure 21 shows the

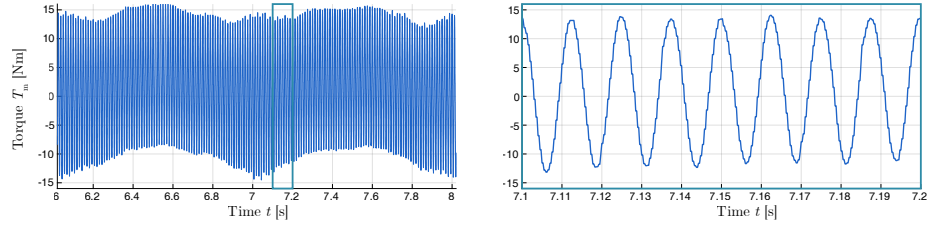


Figure 20: Torque command value

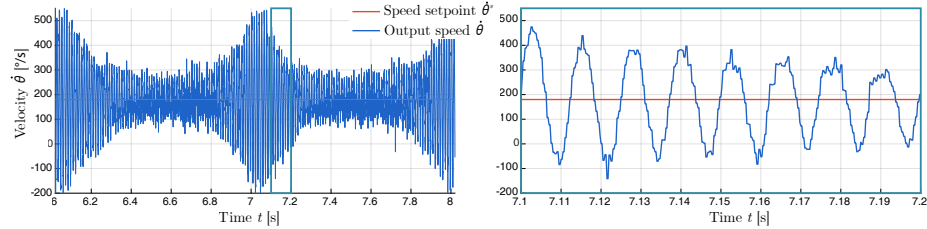


Figure 21: Measured speed and the speed setpoint

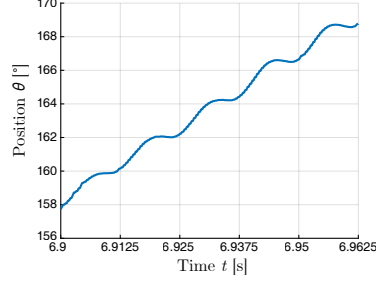


Figure 22: Measured position (close-up of 5 SDFT windows)

measured speed $\dot{\theta}$, together with the setpoint $\dot{\theta}^*$. In figure 22, a close-up view of the measured position θ is shown. When comparing the measured signals with the equivalent signals obtained through co-simulation in figures 12, 13 and 14 it is clear that the system behaviour during the estimation routine is very similar, except for the obvious noise.

In figure 23, the results of the proposed SDFT approach for online tracking of varying inertia are presented. In the case of $f = 160$ Hz the estimated inertia is completely wrong. This confirms that the frequency must be selected inside the region of interest and choosing a higher frequency with the intention to limit

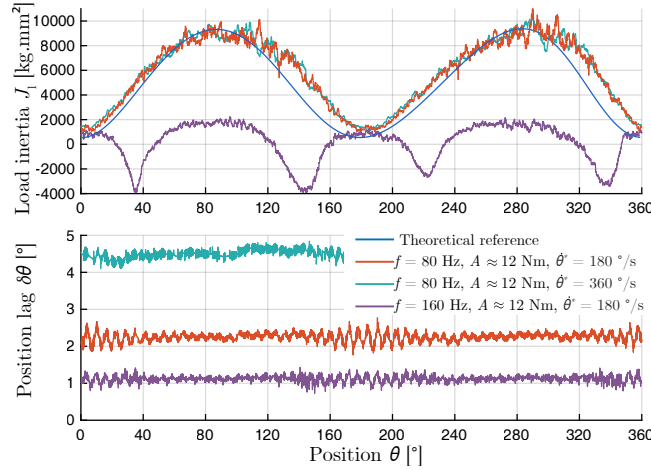


Figure 23: Online tracking of the load inertia with the settings in Table 4

the position lag $\delta\theta$ is not valid.

In the case of $f = 80$ Hz a clear correspondence is found with the theoretical reference and therefore the approach is proven to be valid, even in noisy conditions. The inherent error due to the position lag $\delta\theta$ is again clearly present. However, despite the doubled speed of $\dot{\theta}^* = 360$ °/s compared with $\dot{\theta}^* = 180$ °/s and thus doubled lag, the tracking error is rather the same. As indicated with the sensitivity analysis in section 5.4, the uncertain values of flexibility k and damping b lead to an estimation that is smoother and more accurate at low inertia than at high inertia.

7. Conclusion

This paper presented a SDFT approach for online tracking of rapidly varying inertia. The feasibility of the method has been verified on an industrial machine and its CAD equivalent, modelled in a multibody dynamics software package. A theoretical reference of the inertia variation has been derived from the kinetic energy of a theoretical model of the machine. This theoretical approach has proven to be time-consuming and requires the knowledge of the mass properties of all linkages of the mechanism, which motivates online estimation.

Based on the results, the online SDFT approach is valid for both real machines and their CAD equivalent. The conditions for proper performance are clarified and a summarizing flowchart is given in the appendix. An inherent property of the SDFT is the lagging behaviour. By respecting the proposed guidelines, the estimation errors due to this lagging behaviour can be limited.

Furthermore it has been proven that the SDFT can track the system response online without any prior known mechanical parameters. Still, the conversion from the system response to the inertia requires information concerning the mechanical load. However, the presented guidelines prove that the number of prior known mechanical parameters can be reduced. For example, the approach

is valid for machines containing kinetic friction without having information of this mechanical parameter.

Nonetheless, a drawback is that values of the stiffness and damping of an equivalent spring-damper coupling between rotor and load must be known in advance. Even a rough estimation of these parameters leads to an accurate result of the inertia profile in 1 second. A sensitivity analysis confirms that the remaining inaccuracy of the estimated profile is mainly due to these uncertain values.

When comparing the proposed method with existing methods like the recursive least-squares algorithm the main progresses are that the mechanical parameter is directly estimated leading to faster convergence, noise has nearly no influence on the estimation and less prior known parameters are needed. The SDFT approach is thus considered as a contribution towards fast and accurate estimation of rapidly varying mechanical parameters.

Finally, the developed estimation algorithm has proven to be implementable in a commercial real-time platform.

8. Appendix

8.1. Kinematic relations

By considering three kinematic loops, ABC , $DEGF$ and $ABCD$ (see figure 2), the kinematic relations are found with complex vector analysis of planar mechanisms with multiple loops [30]. After position analysis, the geometric relations are:

$$\theta_3 = \theta_4 = 2 \tan^{-1} \left(\frac{-b - \sqrt{b^2 - 4ac}}{2a} \right) \quad (30)$$

$$\theta_2 = \sin^{-1} \left(\frac{|AB| \sin(\theta_1) + y_c}{|CB|} \right) \quad (31)$$

$$x_c = -x_f - |DC| \sin(\theta_5) - |FD| \cos(\theta_3) \quad (32)$$

$$y_c = -y_f - |DC| \sin(\theta_5) - |FD| \sin(\theta_3) \quad (33)$$

After taking the continuous derivative, the velocity relations are found:

$$\dot{\theta}_3 = \dot{\theta}_4 = \frac{|AB|\sin(\theta_1 - \theta_2)}{|FD|\sin(\theta_3 - \theta_2)} \dot{\theta}_1 \quad (34)$$

$$\dot{\theta}_2 = \frac{|AB|\sin(\theta_1 - \theta_3)}{|CB|\sin(\theta_2 - \theta_3)} \dot{\theta}_1 \quad (35)$$

$$\dot{x}_c = \left(-|AB|\sin(\theta_1) + \frac{|AB|\sin(\theta_1 - \theta_3)}{\sin(\theta_2 - \theta_3)} \sin(\theta_2) \right) \dot{\theta}_1 \quad (36)$$

$$\dot{y}_c = \left(-\frac{|AB|\sin(\theta_1 - \theta_3)}{\sin(\theta_2 - \theta_3)} \cos(\theta_2) + |AB|\cos(\theta_1) \right) \dot{\theta}_1 \quad (37)$$

Note that the distance between two joints of the same link are geometric constants. For example, $|AB|$ in (31), which is the distance between joints A and B is a constant. Also note that the angle θ_5 , as depicted in figure 2, is a geometric constant. In (30) and (31), a , b and c are auxiliary variables:

$$a = -h_1 - h_5 - \cos(\theta_1)(1 + h_3) - h_4\sin(\theta_1) \quad (38)$$

$$b = 2(\sin(\theta_1) + h_2) \quad (39)$$

$$c = h_1 - h_5 + \cos(\theta_1)(1 - h_3) - h_4\sin(\theta_1) \quad (40)$$

In (38), (39) and (40), h_1 , h_2 , h_3 , h_4 and h_5 are auxiliary constants:

$$h_1 = -\frac{x_f - |DC|\cos(\theta_5)}{|AB|} \quad (41)$$

$$h_2 = -\frac{y_f - |DC|\sin(\theta_5)}{|AB|} \quad (42)$$

$$h_3 = -\frac{x_f - |DC|\cos(\theta_5)}{|FD|} \quad (43)$$

$$h_4 = -\frac{y_f - |DC|\sin(\theta_5)}{|FD|} \quad (44)$$

$$h_5 = \frac{|AB|^2 + |FD|^2 - |CB|^2 + (-y_f - |DC|\sin(\theta_5))^2 + (-x_f - |DC|\cos(\theta_5))^2}{2|AB||FD|} \quad (45)$$

The kinematic relations are now solved and can be used for the theoretical derivation of the reference inertia profile in section 2.

8.2. Flowchart

A summarizing flowchart for online tracking of varying inertia is given in figure 24. The first step is to obtain the mechanical load parameters of the

simplified two-mass system. The rotor inertia J_r is found in a data-sheet of the motor. An option for finding the values of the stiffness k and damping b of the spring-damper coupling between rotor and load is through a model fit with a measured frequency response of the machine. The measurement is done at the position θ_{\max} of maximum inertia because the additional frequency f is also selected based on this characteristic in the next step.

The position θ_{\max} of maximum inertia corresponds to the position where the distance from the centre of mass of all linkages to the driven joint is largest. By considering this property, the position θ_{\max} is easily found for simple mechanisms like for instance a crank-shaft mechanism. But for more

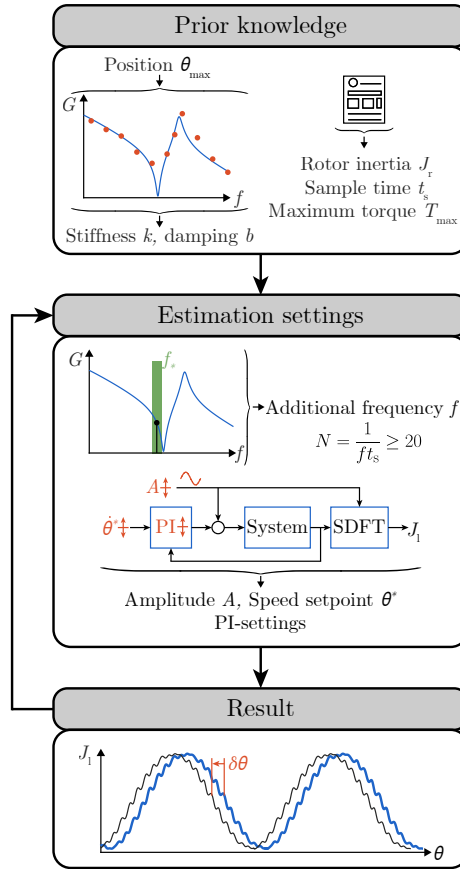


Figure 24: Flowchart for online tracking of varying inertia

complex mechanisms like the pick and place unit, the location of the centre of mass is difficult to imagine. If a CAD model is available, the position θ_{\max} is found with motion simulations [31]. If not, an alternative is to measure the frequency response at multiple positions. The position θ_{\max} of maximum inertia then corresponds with the position where the antiresonance is lowest.

Also a few practical limitations need to be known in advance. The maximum motor torque T_{\max} is found in a data-sheet of the motor. From a manual of the real-time platform, the sample time t_s is found.

Next, the estimation settings are tuned. The additional frequency f is selected in the region of interest f_* (located slightly before the antiresonance frequency at the position of maximum inertia) while considering that the number of samples N must be an integer value greater than 20. Afterwards, the PI-settings of the speed controller are tuned without the additional torque signal activated. The remaining settings, being the amplitude A of the additional torque and the speed setpoint $\dot{\theta}^*$ are then experimentally tuned by using a co-simulation with the CAD equivalent. But if desired, the settings can be directly tuned on the real machine.

The final step is to execute the inertia estimation algorithm online and evaluate the result. Based on the expected position lag $\delta\theta$, the estimation settings can be re-tuned. This iteration is depicted with the recurring line in the flowchart.

References

- [1] H. Dresig, F. Holzweibig, Dynamics of Machinery: Theory and Applications, Springer Science & Business Media, New York, 2010.
- [2] F. Roos, H. Johansson, J. Wikander, Optimal selection of motor and gearhead in mechatronic applications, Mechatronics 16 (2006) 63–72.
- [3] M. S. Huang, Y. L. Hsu, R. F. Fung, Minimum-energy point-to-point

- trajectory planning for a motor-toggle servomechanism, *IEEE/ASME Transactions on Mechatronics* 17 (2012) 337–344.
- [4] Y. L. Hsu, M. S. Huang, R. F. Fung, Energy-saving trajectory planning for a toggle mechanism driven by a PMSM, *Mechatronics* 24 (2014) 23–31.
 - [5] Y.-L. Hsu, Adaptive Tracking Control of a PMSM-Toggle System with a Clamping Effect, *International Journal of Mechanical Engineering and Applications* (2016) 1–10.
 - [6] N. V. Oosterwyck, F. Vanbecelaere, M. Haemers, D. Ceulemans, K. Stockman, S. Derammelaere, Cad enabled trajectory optimization and accurate motion control for repetitive tasks, *IEEE 15th International Conference on Control and Automation (ICCA)* (2019) 387–392.
 - [7] A. Wahrburg, E. Jelavic, S. Klose, K. D. Listmann, Robust Semi-Automatic Identification of Compliantly Coupled Two-Mass Systems, *IFAC* (2017) 14569–14574.
 - [8] R. Pintelon, J. Schoukens, FRF Measurement of Nonlinear Systems Operating in Closed Loop, *IEEE Transactions on Instrumentation and Measurement* (2013) 1334–1345.
 - [9] S. Villwock, M. Pacas, T. Eutebach, Application of the welch-method for the automatic parameter identification of electrical drives, *IECON* (2005) 1449–1454.
 - [10] M. Calvini, M. Carpita, A. Formentini, M. Marchesoni, PSO-based self-commissioning of electrical motor drives, *IEEE Transactions on Industrial Electronics* 62 (2015) 768–776.
 - [11] R. Garrido, A. Concha, Inertia and Friction Estimation of a Velocity-Controlled Servo Using Position Measurements, *IEEE Transactions on Industrial Electronics* (2014) 4759–4770.

- [12] I. Eker, Experimental on-line identification of an electromechanical system, *ISA Transactions* 43 (2004) 13–22.
- [13] P. Kshirsagar, D. Jiang, Z. Zhang, Implementation and Evaluation of Online System Identification of Electromechanical Systems Using Adaptive Filters, *IEEE Transactions on Industry Applications* 52 (2016) 2306–2314.
- [14] N. Nevaranta, J. Parkkinen, T. Lindh, M. Niemela, O. Pyrhonen, J. Pyrhonen, Online Estimation of Linear Tooth-belt Drive System Parameters, *IEEE Transactions on Industrial Electronics* 62 (2015) 7214–7223.
- [15] S. E. Saarakkala, M. Hinkkanen, Identification of Two-Mass Mechanical Systems Using Torque Excitation: Design and Experimental Evaluation, *IEEE Transactions on Industry Applications* 51 (2015) 4180–4189.
- [16] F. Schutte, S. Beineke, A. Rolfsmeier, H. Grotstollen, Online identification of mechanical parameters using extended Kalman filters, *IEEE* (1997) 501–508.
- [17] M. Perdomo, M. Pacas, T. Eutebach, J. Immel, Identification of Variable Mechanical Parameters using Extended Kalman Filters, 2013 9th IEEE International Symposium on Diagnostics for Electric Machines, Power Electronics and Drives (SDEMPED) (2013) 377–383.
- [18] M. Goubey, Kalman filter based observer design for real-time frequency identification in motion control systems, 20th International Conference on Process Control (2015) 296–301.
- [19] N. Nevaranta, S. Derammelaere, J. Parkkinen, B. Vervisch, T. Lindh, M. Niemela, O. Pyrhonen, Online Identification of a Two-Mass System in Frequency Domain using a Kalman Filter, *Modeling, Identification and Control* 37 (2016) 133–147.
- [20] E. Jacobsen, R. Lyons, The sliding DFT, *IEEE Signal Processing Magazine* 20 (2003) 74–80.

- [21] E. Jacobsen, R. Lyons, An Update to the Sliding DFT, *IEEE Signal Processing Magazine* 21 (2004) 110–111.
- [22] K. Duda, Accurate, Guaranteed Stable, Sliding Discrete Fourier Transform [DSP Tips & Tricks], *IEEE Signal Processing Magazine* 27 (2010) 124–127.
- [23] S. Derammelaere, C. Debruyne, F. De Belie, K. Stockman, L. Vandeveldel, Load angle estimation for two-phase hybrid stepping motors, *IET Electric Power Applications* 8 (2014) 257–266.
- [24] N. Nevaranta, S. Derammelaere, J. Parkkinen, B. Vervisch, T. Lindh, K. Stockman, M. Niemela, O. Pyrhonen, J. Pyrhonen, Online Identification of a Mechanical System in Frequency Domain Using Sliding DFT, *IEEE Transactions on Industrial Electronics* 63 (2016) 5712–5723.
- [25] J. De Viaene, S. Derammelaere, K. Stockman, Load angle estimation for dynamic stepping motor motion applications, *Mechatronics* 53 (2018) 229–240.
- [26] R. C. Hibbeler, Chapter 18: Planar Kinetics of a Rigid Body: Work and Energy, in: *Engineering Mechanics: Dynamics*, 14th Edition, Pearson, 2016, pp. 472–515.
- [27] BECKHOFF, TC3 Bode Plot Manual, 2017, p. 46.
- [28] S. Villwock, M. Pacas, Application of the Welch-Method for the Identification of Two- and Three-Mass-Systems, *IEEE Transactions on Industrial Electronics* (2008) 457–466.
- [29] M. A. Valenzuela, J. M. Bentley, R. D. Lorenz, Evaluation of torsional oscillations in paper machine sections, *IEEE Transactions on Industry Applications* 41 (2005) 493–501.
- [30] W. L. Cleghorn, N. Dechev, *Mechanisms of Machines*, Oxford University Press, 2016.

- [31] G. Berselli, F. Balugani, M. Pellicciari, M. Gadaleta, Energy-optimal motions for Servo-Systems: A comparison of spline interpolants and performance indexes using a CAD-based approach, *Robotics and Computer-Integrated Manufacturing* 40 (2016) 55–65.